PLANT SCIENCES

Functional divergence of plant SCAR/WAVE proteins is determined by intrinsically disordered regions

Sabine Brumm†, Aleksandr Gavrin‡, Matthew Macleod, Guillaume Chesneau§, Annika Usländer¶, Sebastian Schornack*

Dynamic actin cytoskeleton reorganization enables plant developmental processes requiring polarized transport such as root hair and leaf trichome formation. The SCAR/WAVE complex plays a crucial role in regulating these dynamics through ARP2/3-mediated actin branching. *SCAR/WAVE* genes occur as small families across a wide range of plant species, but whether and how they fulfill different functions remains unclear. We use a systematic chimera approach to define the differential functionality of two closely related *Medicago truncatula* SCAR proteins in plant development. We show that SCAR/WAVE contribution to *M. truncatula* root hair or *Arabidopsis thaliana* trichome formation is dependent on two central intrinsically disordered regions (IDRs). Differential functionalities of *M. truncatula* SCAR proteins were furthermore associated with the presence/absence of a 42–amino acid sequence within the IDR that affected protein stability. Through uncovering a molecular basis for functional differences, we advance our understanding of plant SCAR/WAVE complexes.

INTRODUCTION

Directional protein transport of endomembrane vesicles along the actin cytoskeleton network is central to plant growth, development, and interactions with the environment (*1*–*4*). In eukaryotes, dynamic actin cytoskeleton organization is finely tuned by two conserved molecular complexes. The Actin-Related Protein 2/3 (ARP2/3) protein complex controls the formation of branched actin filaments (*5*, *6*). Actin branching is pivotal for plant development, and ARP2/3 component mutants display diverse cell polarity related phenotypes (*7*–*10*). The ARP2/3 complex is regulated by the SCAR/WAVE (suppressor of cAMP receptor/WASP family verprolin homologous) complex, which includes the conserved proteins PIR/SRA1, NAP1/NAP125, BRICK1/HSPC300, and one of the several ABIL and SCAR proteins (*11*). Mutations in SCAR/WAVE complex components similarly lead to defects in cell morphology, division, expansion, and adhesion, with severity depending on the affected subunit (*12*–*19*). In *Arabidopsis thaliana* (*A. thaliana*; *At*), single-gene mutations in the core SCAR/WAVE complex components (*PIR*, *NAP1*, and *BRICK1*) cause similar developmental defects to *arp2/3* loss-of-function mutations (*14*–*16*), whereas plants with single mutations of any of the multicopy *ABIL* and *SCAR* subunits exhibit milder phenotypes (*13*, *17*, *18*). Among the four *A. thaliana SCAR* genes (*AtSCAR1-4*), only *scar2* mutants display the characteristic *ARP2/3*-related trichome phenotype (*12*), but genetic studies suggest that *AtSCAR1-4* function redundantly with varying contributions (*13*, *17*). A threshold model has been proposed in which *AtSCAR* expression levels and biochemical properties dictate their roles in different tissues (*17*). However, the molecular basis for these differences remains poorly understood.

All plant SCAR proteins have terminal conserved domains but carry a large and highly variable central region (*11*). The N-terminal "SCAR-homology-domain" (SHD) of *A. thaliana* SCARs physically interacts with ABIL1 and BRK1 (*12*, *18*). The C-terminal "Wiskott-Aldrich homology 2, central, and acidic" (WA) domain of plant SCAR proteins activates the ARP2/3 complex (*12*, *13*, *20*). Beyond their well-characterized functional domains, many actin regulatory proteins contain intrinsically disordered regions (IDRs) (*21*). IDRs often serve as hubs for protein-protein interactions and are frequently enriched in posttranslational modification (*22*, *23*). Las17, the yeast homolog of WASP—a protein class that includes SCAR/WAVE (*24*)—has a central IDR with a proline-rich region that interacts with the Src homology domain 3 of myosin I motor proteins and promotes actin polymerization (*25*, *26*). Unlike vertebrate WAVE proteins, which also feature a central proline-rich region (*24*), plant SCARs lack an extensive proline-rich segment (*11*). Whether the variable central regions may serve a regulatory role analogous to IDRs in other actin-associated proteins and contributes to SCAR functionality in plants still needs to be experimentally addressed.

In *Medicago truncatula* (*M. truncatula*; *Mt*), *API* (*Aberrant Primordia Invasion*) is the only *SCAR* gene that has been functionally characterized to date (*19*). *MtAPI* is a close homolog of *AtSCAR2*. *MtAPI* mutants have shorter root hairs, enhanced resistance to Phytophthora infection, and are impaired in root nodule symbiosis with nitrogen fixing bacteria (*19*, *27*). The function of *MtAPI* in *M. truncatula* can be substituted by its *A. thaliana* counterpart, *AtSCAR2* (*19*). However, it remains uncertain whether *MtAPI* can reciprocally replace the functionality of *AtSCAR2* in *A. thaliana* plants. *M. truncatula* also encodes two additional *Homologs of API* (*HAPI1* and *HAPI2*); *Mt*HAPI1 is more closely related to *Mt*API than *Mt*HAPI2. However, whether these *M. truncatula* SCAR proteins share the same function or have distinct roles has not been addressed yet.

In this study, we investigated the two closely related *SCAR* genes, *MtAPI* and *MtHAPI1*, with a specific focus on the role of their central variable regions in determining their functionality in *M. truncatula* roots and *A. thaliana* leaves. We discovered that *MtHAPI1* cannot functionally replace its close homolog *MtAPI* as it is unable to complement the *api* mutant. *MtHAPI1* but not *MtAPI* can complement

Sainsbury Laboratory (SLCU), University of Cambridge, 47 Bateman Street, Cambridge CB2 1LR, UK.
*Corresponding author. Email: sebastian.schornack@slcu.cam.ac.uk
†Present address: Department of Phytopathology, TUM School of Life Sciences, Technische Universität München, Freising-Weihenstephan, Germany.
‡Present address: Department of Molecular Biology and Genetics, Aarhus University, Aarhus, Denmark.
§Present address: Department of Plant Microbe Interactions, Max Planck Institute for Plant Breeding Research, 50829 Cologne, Germany.
¶Present address: MLL Münchner Leukämielabor GmbH, Munich, Germany.

A. thaliana defective in *AtSCAR2*. This assigns divergent functions to both *M. truncatula SCAR* genes. Using a chimera approach, our research revealed the significance of two IDRs within the large central domain of *Mt*API and *Mt*HAPI1, emphasizing the crucial role of this domain in dictating functionality. Furthermore, a destabilizing element present in *Mt*API and missing in *Mt*HAPI1 governs SCAR protein abundance in *A. thaliana*. Our findings provide direct evidence that the variable central regions of plant SCAR proteins play a pivotal role in defining their functionality. By leveraging the distinct properties of *M. truncatula* homologs, we document how closely related SCAR/WAVE proteins can exert different functionality via variation in two intrinsically disordered domains. These insights advance our understanding of SCAR protein specificity and the broader mechanisms governing ARP2/3 activation in plants.

RESULTS

Paralogous *M. truncatula* SCAR/WAVE proteins differ in their functionality

Our previous *M. truncatula* research has shown that *AtSCAR2* and the *Lotus japonicus* homolog *SCARN* can substitute *MtAPI* functionality when expressed in *M. truncatula* roots (*19*), suggesting functional conservation. Phylogenetic analysis shows that *At*SCAR2 is closely related to *Mt*API and *Mt*HAPI1 (Fig. 1A), raising the question whether *Mt*API and *Mt*HAPI1 have similar functions. The second, more distantly related homolog *MtHAPI2* was excluded from this study.

To test whether *MtHAPI1* can functionally replace *MtAPI*, we introduced *MtHAPI1* under control of a 2-kb long *MtAPI* promoter sequence (*19*) into roots of *M. truncatula api*. In this *api* mutant background, *MtHAPI1* was expressed at substantially higher levels (fig. S1A) compared to roots transformed with green fluorescent protein (GFP) and had higher transcript levels than *MtAPI* (fig. S1B). Despite its high transcript levels, *MtHAPI1* did not complement the short root hair length phenotype of the *api* mutant (Fig. 1, B and C) whereas the 2-kb promoter-driven *MtAPI* did (*19*). Thus, *MtHAPI1* cannot substitute for the *MtAPI* root hair development function in *M. truncatula*.

Next, we tested whether *MtAPI* and *MtHAPI1* could substitute for the loss of *AtSCAR2/DISTORTED3* in the *A. thaliana dis3-4* mutants (*12*). These plants have normally developed root hairs but display distorted trichome phenotypes. We introduced *MtAPI*, *MtHAPI1*, and *AtSCAR2*, all under the *A. thaliana UBIQUITIN3* (*AtUBQ3*) promoter, into *dis3-4* (Fig. 1, D and E, and fig. S1, C and D). In this context, *MtHAPI1* and *AtSCAR2* successfully rectified the trichome development defects of *A. thaliana dis3-4* whereas *MtAPI*-expressing plants developed distorted trichomes (Fig. 1, D and E, and fig. S1D). Together, these results suggest that *M. truncatula MtAPI* and *MtHAPI1* are phylogenetically close but differ in their functional specificity.

*Mt*API and *Mt*HAPI1 specificity is encoded within two IDRs

To determine the molecular basis underpinning functional differences of *Mt*API and *Mt*HAPI1, we analyzed their protein sequences and systematically assessed the function of API/HAPI1 chimeric proteins (Fig. 2 and figs. S2 and S3). A comparison of the *Mt*API and *Mt*HAPI1 protein sequences revealed five distinct regions of varying sequence similarity. The first, third, and fifth regions exhibited high sequence conservation, whereas the second and fourth regions displayed greater variability including amino acid segments missing in *Mt*HAPI1 (fig. S2A). The IUPred3a web server (https://iupred3.elte.hu/) predicts a high probability for intrinsic disorder (scores between 0.5 and 1) in regions 1 (post-SHD domain), 2, 4, and 5 (fig. S2, B and C). Given the conservation of the SHD and WA domains in regions 1 and 5, associated with SCAR/WAVE complex interaction and ARP2/3 activation (*12*, *13*, *20*), respectively, we hypothesized that variation within regions 2 and 4 may account for the differential specificity.

To identify regions with functional specificity in *M. truncatula* and *A. thaliana*, we exchanged region 2, region 4, or both regions between the two paralogs (Fig. 2A). Expression of the resulting chimeric proteins under the *MtAPI* promoter in *M. truncatula api* roots revealed that swapping a single region between *Mt*API and *Mt*HAPI1 was insufficient to alter their functionality (Fig. 2, B and C, and fig. S3). However, when regions 2 and 4 were swapped together, *Mt*API failed to confer normal root hair development having significantly shorter root hairs, whereas *Mt*HAPI1 gained functionality in root hair development (Fig. 2, D and E, and fig. S3). Hence, *Mt*API regions 2 and 4 both contribute to its functionality in *M. truncatula* root hair development.

We next analyzed the chimeras for their ability to rescue the trichome defects of the *A. thaliana dis3-4* mutant. Exchanging a single region between *Mt*API and *Mt*HAPI1 did not alter their functionality (Fig. 2, F and G, and fig. S3). However, the simultaneous exchange of regions 2 and 4 compromised *Mt*HAPI1 functionality in *A. thaliana*, whereas comparable *Mt*API chimeras rescued the trichome development defects of the *dis3-4* mutant defective in *AtSCAR2*. We therefore conclude that *Mt*HAPI1 regions 2 and 4 together condition function in *A. thaliana* trichome development.

Taking the data from *M. truncatula* and *A. thaliana* together, we demonstrated that exchanging regions 2 and 4 between *Mt*API and *Mt*HAPI1 exchanges their functionality.

Specific amino acids, not protein length, determine *Mt*SCAR specificity

To better understand how SCAR sequence variation contributes to the distinct molecular functionalities of *Mt*API and *Mt*HAPI1, we generated an extended phylogenetic tree of SCAR proteins derived from nine different legume genomes (fig. S4A). To further curate our comparison, we focused solely on *Mt*API and *Mt*HAPI-like protein sequences and removed all *Mt*HAPI2-like sequences from subsequent alignments. This comparative analysis revealed that all *Mt*HAPI1-like proteins lack a 42–amino acid segment at the intersection of *Mt*API regions 1 and 2 (Segment A), as well as two segments of 20 (Segment B) and 29 (Segment C) amino acids in *Mt*API region 4 (fig. S4B), resulting in an overall shorter length. Some amino acid residues within these API-like segments are highly conserved, and others vary notably between the different species (fig. S5).

To investigate whether differential *Mt*API and *Mt*HAPI1 functionality is influenced by their overall length or protein sequence composition, we either swapped all identified amino acid segments between *Mt*API and *Mt*HAPI1 or substituted them with the glycine/serine (GS) linkers of the same length (Fig. 3A). An mCitrine tag introduced into a permissive site (*28*) within region 2 of all *Mt*API and *Mt*HAPI1 variants allowed us to also assess localization and abundance of these protein variants.

First, we tested whether *Mt*API protein segments A, B, and C are essential for *Mt*API functionality in *M. truncatula* root hairs. To that end, we expressed the deletion and GS linker constructs under

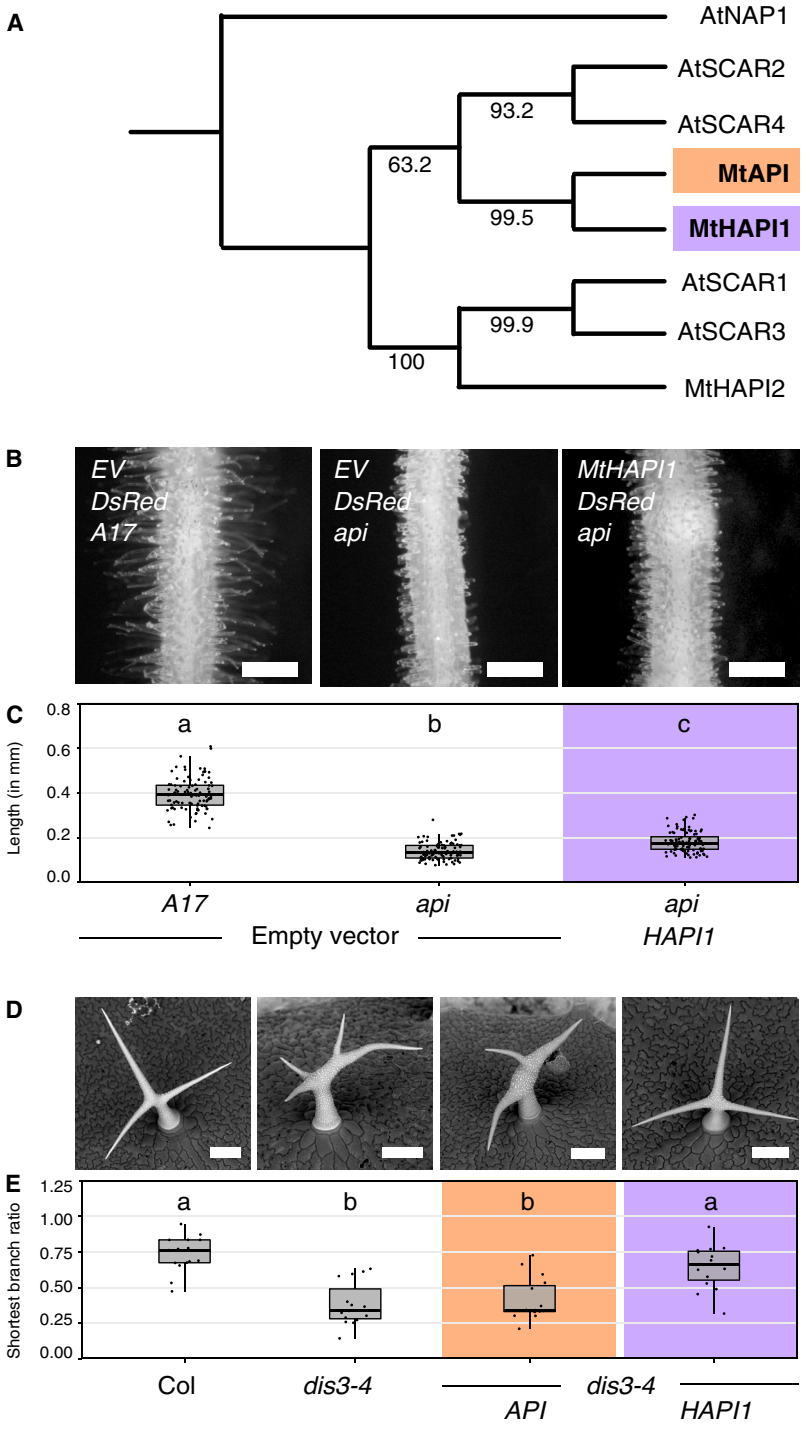

Fig. 1. Two closely related *M. truncatula* SCAR proteins exhibit different functions. (**A**) Maximum likelihood phylogenetic tree of *A. thaliana* and *M. truncatula* SCAR proteins with AtNAP1 as an out-group. *M. truncatula* proteins of interest in this study: *Mt*API (orange, bold) and *Mt*HAPI1 (purple, bold). Node bootstrap values are shown. (**B**) Epifluorescence microscopy images of transgenic *API* and *api M. truncatula* hairy roots expressing an empty *pAtUBQ10:dsRed* vector control or coexpressing *pAtUBQ10:dsRed* with *MtHAPI1* under control of the *MtAPI* promoter. Scale bars, 0.5 mm. (**C**) Root hair length measurements in millimeters (mm). Each dot represents one measurement ($n = 100$ per genotype). For each genotype, 20 root hairs (technical replicates) across five independently transformed roots (biological replicates) were measured. Statistics: Shapiro-Wilk test, followed by Kruskal-Wallis with Bonferroni correction; significance differences are indicated by letters a, b, and c. (**D**) Scanning electron micrographs of *A. thaliana* trichomes from Col, *dis3-4*, and *dis3-4* lines transformed with *MtHAPI1* or *MtAPI* driven by *AtUBQ3* promoter. Scale bars, 90 μm. (**E**) Shortest trichome branch ratios ($n = 15$ per genotype). Each dot represents the shortest branch ratio of one trichome. Five trichomes per leaf (technical replicates) from three independently grown plants (biological replicate) were analyzed. Statistics: Shapiro-Wilk test, followed by Kruskal-Wallis with Bonferroni correction; significance differences are indicated by letters a and b.

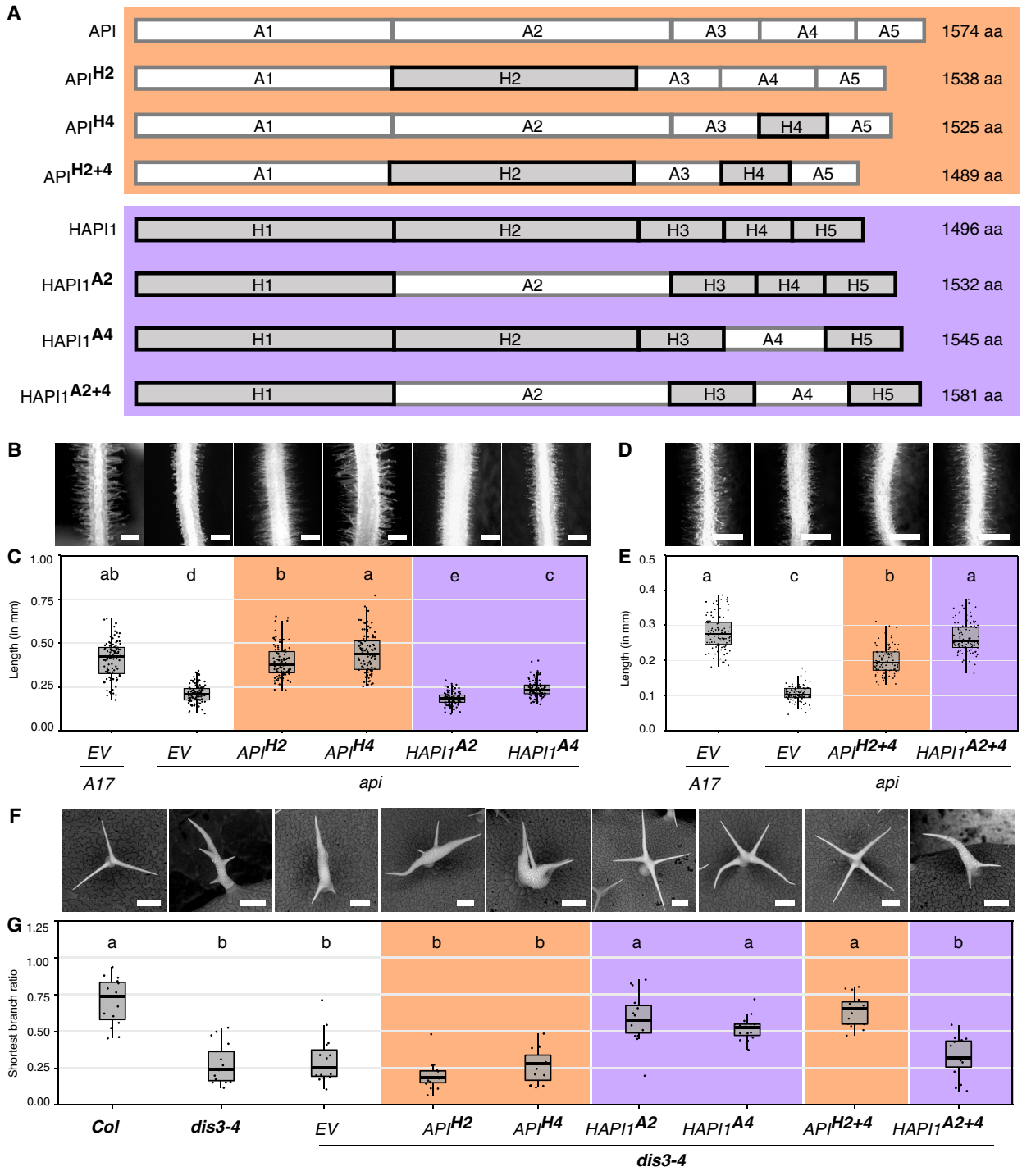

Fig. 2. Exchanging two regions between *Mt*API and *Mt*HAPI1 switches their functions. (**A**) Schematic of *Mt*API (orange) and *Mt*HAPI1 (purple) chimeric proteins, with *Mt*API regions in white and *Mt*HAPI1 in gray. aa, amino acids. (**B** to **E**) Epifluorescence microscopy images of transgenic *M. truncatula API (A17)* and *api* hairy roots expressing an empty *pAtUBQ10:dsRed* vector control or coexpressing *pAtUBQ10:dsRed* with chimeric *MtAPI/HAPI1* variants [region 2 or 4 exchanged in (B); both in (D)] under the *MtAPI* promoter. Scale bars, 0.5 mm. Root hair length measurements of *api* roots with single region (C) or double region (E) *MtAPI/MtHAPI1* chimeras. Each dot represents one measurement ($n = 100$ per genotype). For each genotype, 20 root hairs (technical replicates) across five independently transformed roots (biological replicates) were measured. Statistics: Shapiro-Wilk test, followed by Kruskal-Wallis with Bonferroni correction; significance differences are indicated by letters a, ab, b, c, d, and e. (**F**) Scanning electron micrographs of *A. thaliana* trichomes from untransformed Col, *dis3-4*, and *dis3-4* lines expressing *empty vector* (EV) or chimeric *MtAPI/HAPI1* variants under the *AtUBQ3* promoter. Scale bars, 90 μm. (**G**) Shortest trichome branch ratios ($n = 15$ per genotype). Each dot represents the shortest branch ratio of one trichome. Five trichomes per leaf (technical replicates) from three independently grown plants (biological replicate) were analyzed. Statistics: Shapiro-Wilk test, followed by Kruskal-Wallis with Bonferroni correction; significance differences are indicated by letters a and b. Orange: *MtAPI* chimeras; Purple: *MtHAPI1* chimeras.

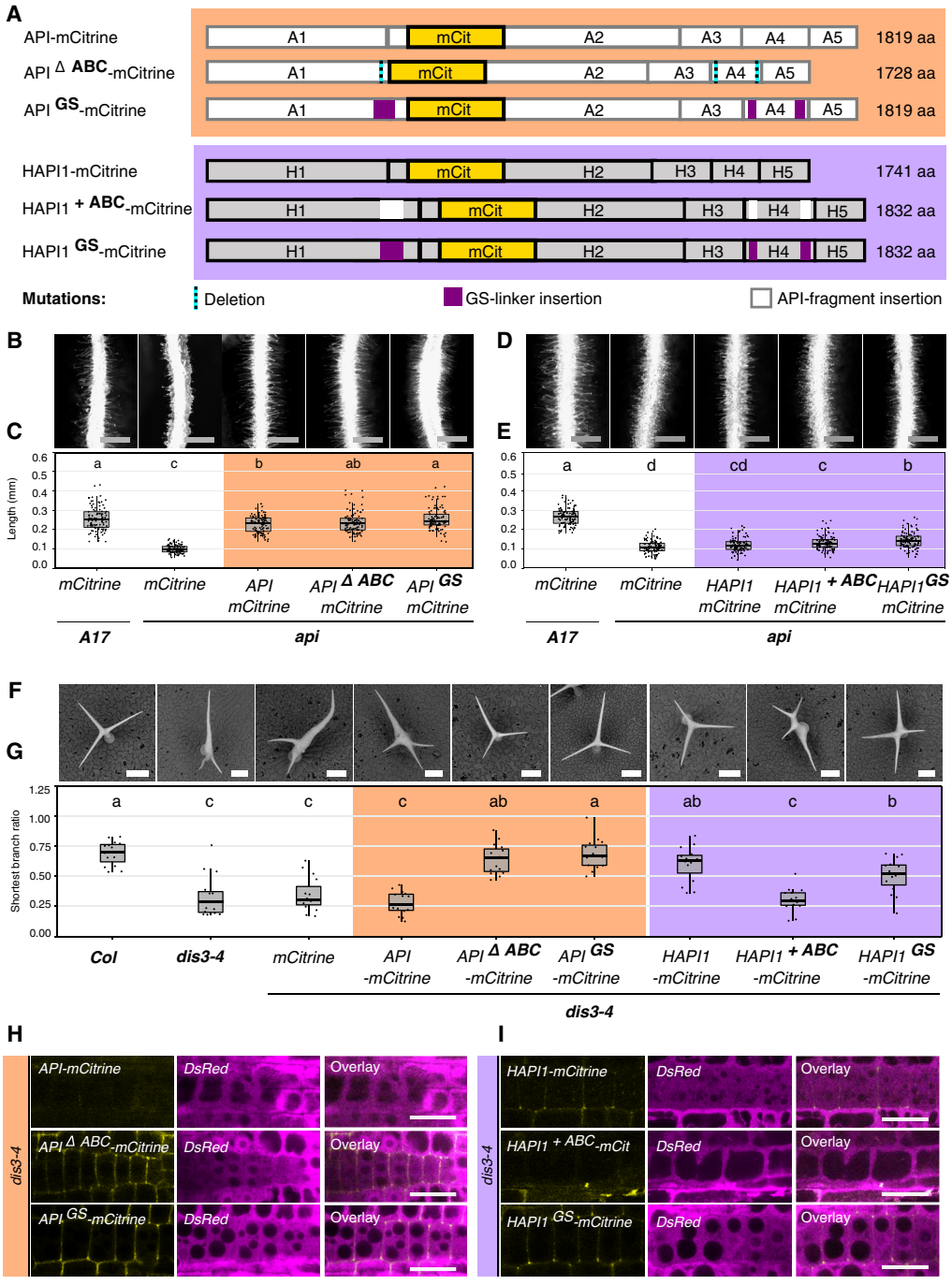

Fig. 3. Three *Mt*API amino acid segments contribute to functional separation. (**A**) Schematic of *Mt*API (orange) and *Mt*HAPI1 (purple) segments A, B, and C mutant protein variants with fluorescent tags. Segments A, B, and C in *Mt*API are either deleted (dotted lines on cyan) or replaced with GS linkers (magenta). In *Mt*HAPI1, *Mt*API segments A, B, and C (white) or GS linkers are inserted. mCitrine tags are shown in yellow, with protein size changes indicated. (**B** to **E**) Epifluorescence microscopy images of *M. truncatula A17* and *api* roots, coexpressing *MtAPI* (B) *or MtHAPI1* (D) segment mutants with *pAtUBQ10:dsRed*. Scale bars, 0.5 mm. Root hair length measurements of *MtAPI* (C, orange) or *MtHAPI1* (E, purple) segment mutants in *api* [in millimeters (mm)]. Each dot represents one measurement ($n = 100$ per genotype). For each genotype, 20 root hairs (technical replicates) across five independently transformed roots (biological replicates) were measured. Statistics: Shapiro-Wilk test, followed by Kruskal-Wallis with Bonferroni correction; significance differences are indicated by letters a, b, c, and d. (**F**) Scanning electron micrographs of *A. thaliana* trichomes from *Col*, *dis3-4*, and *dis3-4* lines expressing *MtAPI* or *MtHAPI1* segment variants under the *AtUBQ3* promoter. Scale bars, 90 μm. (**G**) Shortest branch ratios ($n = 15$ per genotype). Each dot represents the shortest branch ratio of one trichome. Five trichomes per leaf (technical replicates) from three independently grown plants (biological replicate) were analyzed. Statistics: Shapiro-Wilk test, followed by Kruskal-Wallis with Bonferroni correction; significance differences are indicated by letters a, b, and c. (**H** and **I**) Representative confocal microscopy images of *Mt*API (H) and *Mt*HAPI1 (I) segment mutant expression and localization (yellow) in *A. thaliana* root cells. *DsRed* (magenta) serves as transformation control and cytosolic marker. Scale bars, 20 μm.

control of the *MtAPI* promoter in roots of *M. truncatula api* composite plants (Fig. 3, B to E). As expected, a wild-type API-mCitrine fusion construct complemented the short root hair phenotype of *api* (Fig. 3, B and C). Removing *Mt*API segments A, B, and C (API$^{\Delta ABC}$-mCitrine) or replacing these segments with GS linkers in *Mt*API (API^{GS}-mCitrine) did not impair *Mt*API functionality (Fig. 3, B and C). Inserting *Mt*API segments A, B, and C or GS linkers into *Mt*HAPI1 (HAPI^{+ABC}-mCitrine; HAPI^{GS}-mCitrine) did not confer the ability to rescue *api* root hair defects (Fig. 3, D and E). We therefore conclude that *Mt*API segments A, B, and C do not define *Mt*API functionality and that other regions of the large central domain likely condition functionality in *M. truncatula* roots.

We next tested the same constructs in the context of *A. thaliana* trichome development (Fig. 3, F and G, and fig. S6). Although *Mt*API does not normally complement distorted trichomes in *A. thaliana dis3-4* mutants, the replacement of *Mt*API segments A, B, and C with GS residue linkers (API^{GS}-mCitrine) or their complete deletion (API$^{\Delta ABC}$-mCitrine) resulted in a gain of function, similar to *Mt*HAPI or *At*SCAR2 (Fig. 3, F and G). API^{delABC}-mCitrine and API^{GS}-mCitrine polarly localized to the plasma membrane in *A. thaliana* root cells, with visible signal accumulation at the cell periphery (Fig. 3H), similar to the known localization of *At*SCAR1 (*29*). By contrast, no API-mCitrine signals were visible at the cell periphery. Unlike wild-type *Mt*HAPI, the insertion of *Mt*API amino acid segments A, B, and C into *Mt*HAPI1 (HAPI^{+ABC}-mCitrine) failed to rescue the *A. thaliana dis3-4* trichome phenotype (Fig. 3, F and G). The substitution of these amino acids with the same number of GS residues (HAPI^{GS}-mCitrine) maintained functionality. In contrast to API-mCitrine, weak HAPI1-mCitrine signals were detectable at the cell peripheries (Fig. 3I). The insertion of GS linkers did not interfere with HAPI1-mCitrine fluorescence, but when we inserted *Mt*API segments A, B, and C into HAPI1-mCitrine, we were no longer able to detect fluorescence signals. Thus, the presence of *Mt*API segments A, B, and C abolishes trichome functionality and diminishes peripheral fluorescence signals. This suggests that three specific amino acid segments in the *Mt*API regions 2 and 4 control specificity, protein levels, and localization in *A. thaliana*.

42–Amino acid *Mt*API sequence destabilizes proteins in Arabidopsis and Nicotiana

To determine the amino acid segments in *Mt*API regions 2 and 4, which prevent complementation of *A. thaliana dis3-4*, we tested additional *Mt*API deletion constructs (Fig. 4, A to C, and fig. S7, A and B). API$^{\Delta A}$-mCitrine significantly restored trichome morphology, albeit not to full extent, whereas API$^{\Delta B}$-mCitrine and API$^{\Delta C}$-mCitrine were indistinguishable from the mCitrine negative control. API$^{\Delta AB}$-mCitrine and API$^{\Delta AC}$-mCitrine fully rescued trichome morphology, whereas API$^{\Delta BC}$-mCitrine significantly but not fully increased the length of the shortest trichome branch compared to the negative controls. Taking the data from fluorescence imaging and trichome morphology together, we conclude that the 42–amino acid sequence of segment A is sufficient to prevent restoration of trichome morphology and to lower *Mt*API protein abundance.

We next tested whether the 42–amino acid sequence of *Mt*API segment A functions independent of the SCAR protein or plant species context. In *Nicotiana benthamiana* (*N. benthamiana*) transient expression experiments under *A. thaliana UBIQUITIN3* promoter control, the fluorescent signal was significantly reduced in 42aa-mCitrine fusions compared to mCitrine alone (Fig. 4, D and E). Replacing the 42 amino acids with a GS linker of equal length did not reduce mCitrine fluorescence levels. Although the transcript levels of mCitrine and 42aa-mCitrine were similar, protein levels differed substantially (Fig. 4, F and G, and fig. S8, A and B). Thus, the addition of a 42–amino acid sequence contained within *Mt*API segment A reduces protein abundance across different proteins, species, and tissue contexts.

Protein stability can be affected by posttranslational modifications, including glycosylation, ubiquitination, and phosphorylation. The 42–amino acid sequence contains several potential posttranslational modification sites (fig. S9, A to E). A glycosylation site was predicted with high confidence for asparagine at position 5 (513 in *Mt*API). Deletion of the asparagine residue in the 42–amino acid mCitrine construct (41aa-mCitrine) reduced mCitrine fluorescence even further (fig. S9, B and C). Mass spectrometry analysis of immunoprecipitated 42aa-mCitrine (fig. S9A and tables S3 and S4) revealed a ubiquitinated lysine residue at position 12 (K520 in *Mt*API) (fig. S9B). However, substituting all lysine residues (9, 10, 12, and 39) to arginine (R) residues (4xKtoR-mCitrine) did not restore mCitrine fluorescence to control levels (fig. S9, B and D). Substituting the corresponding K residues to R in API-mCitrine (K517R, K518R, K520R, and K547R) did not lead to a gain of function of *Mt*API in *A. thaliana* (fig. S10, A to C). Neither the single nor multiple substitution mutant API-mCitrine variants were able to rescue the *A. thaliana dis3-4* distorted trichome phenotype, suggesting that lysine-targeted ubiquitination of the 42–amino acid sequence does not contribute to *Mt*API destabilization in *A. thaliana*.

Further dissection of the peptide into four parts (1 to 21, 22 to 43, 22 to 30, and 31to 43 amino acids) (Fig. 4G and fig. S9B) and their expression as mCitrine fusions in *N. benthamiana* leaves showed that amino acids 22 to 43 drove the most significant reduction of mCitrine fluorescence levels (Fig. 4H). These 22 amino acids include four phosphorylated serine and threonine residues (S22, T23, T28, and S30) (fig. S9B). To abolish phosphorylation or mimic constitutive phosphorylation, we changed them to alanine (A) or aspartic acid (D) residues, respectively, in 42aa-mCitrine (4xSTtoA- and 4xSTtoD-mCitrine) (fig. S9, B and E). None of these modifications resulted in fluorescence levels comparable to mCitrine alone (fig. S9E). We conclude that phosphorylation of the 42 amino acids does not contribute to the decreased fluorescence levels of 42aa-mCitrine. In summary, the results demonstrate that a segment of 42 amino acids lowers protein abundance of *Mt*API and other proteins in *A. thaliana* and *N. benthamiana* via an unidentified mechanism.

In summary, we show that SCAR/WAVE contribution to *M. truncatula* root hair or *A. thaliana* trichome formation is dependent on two central IDRs (Fig. 4I). Differential functionalities of *M. truncatula* SCAR proteins in the context of *A. thaliana* trichome formation were furthermore associated with the presence/absence of a 42–amino acid sequence within an IDR that affected protein stability. Through uncovering a molecular basis for functional differences, we advance our understanding of plant SCAR/WAVE complexes.

DISCUSSION

In this study, we show that two closely related *M. truncatula* SCAR proteins have distinct functional specificities due to differences in two central IDRs. SCAR/WAVE proteins are part of the evolutionary conserved actin regulatory SCAR/WAVE complex in eukaryotes. Although some components of this complex have been retained as single copy genes during evolution, other components, such as

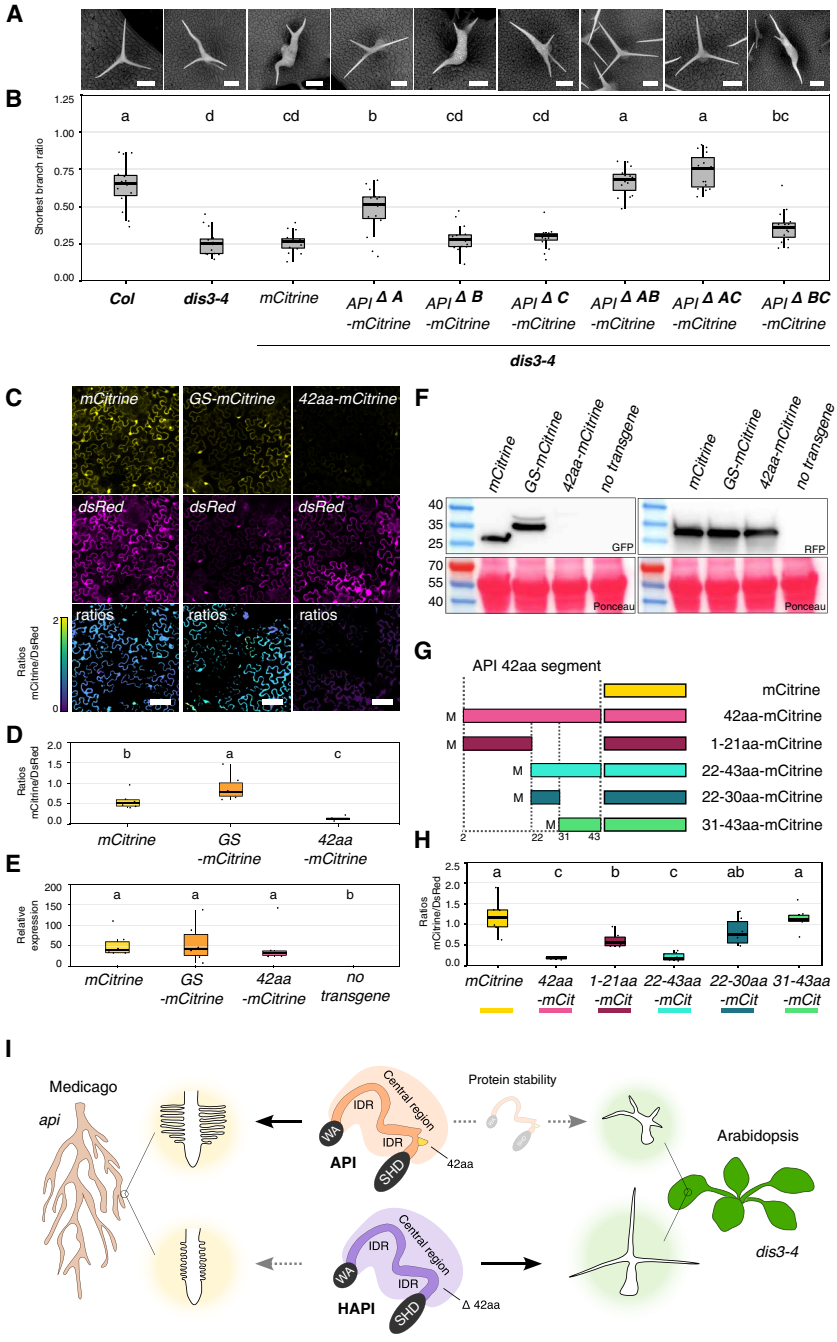

Fig. 4. *Mt*API segment A acts as a destabilizing element. (**A**) Scanning electron microscopy images of *A. thaliana* Col, *dis3-4*, and *dis3-4* lines expressing *MtAPI* segments A, B, and C deletions under the *AtUBQ3* promoter. Scale bars, 90 μm. (**B**) Shortest trichome branch ratio ($n = 15$ per genotype). Five trichomes per leaf (technical replicates) from three plants (biological replicate) were analyzed. Statistics: Shapiro-Wilk, Kruskal-Wallis with Bonferroni correction; significance groups: a, b, bc, cd, and d. (**C**) Confocal images of mCitrine, GS-mCitrine, and 42aa-mCitrine in *N. benthamiana* pavement cells (yellow) with DsRed control (magenta). *Z*-projections of fluorescence ratios shown as false color images. Scale bars, 100 μm. (**D**) mCitrine fluorescence normalized to DsRed ($n = 6$ biological replicates). Statistics: Shapiro-Wilk, Kruskal-Wallis with Bonferroni correction; significance groups: a, b, and c. (**E**) qPCR quantification of *mCitrine* mRNA levels, using 2-ΔΔCP with *NtL23* and *NtFBOX* as references ($n = 6$ biological replicates). Negative control: untransformed leaves. Statistics: Shapiro-Wilk, Kruskal-Wallis with Bonferroni correction; significance groups: a and b. (**F**) Western blot (see fig. S8, A and B) of mCitrine variants and coexpressed DsRed. Negative control: untransformed leaves. Membranes were stained with Ponceau and probed with GFP or RFP antibodies. Expected sizes: Rubisco (55 kDa, Ponceau), DsRed (28 kDa); mCitrine (27 kDa); GS-mCitrine (36 kDa), 42aa-mCitrine (38 kDa). Prestained ladder: Page Ruler (10 to 180 kDa). (**G**) Color-coded schematic of 42aa-mCitrine deletions. Deletion parts are confined by dotted lines, followed by mCitrine tag. (**H**) mCitrine/DsRed fluorescence ratios ($n = 6$ biological replicates). Statistics: Shapiro-Wilk, Kruskal-Wallis with Bonferroni correction; significance groups: a, b, and c. Colors refer to schematic (**I**). Schematic model: Central IDR condition the ability to complement the *api* short root hair phenotype in *M. truncatula*. The presence of 42 amino acids in *Mt*API destabilizes it and prevents functional complementation in *A. thaliana dis3-4* trichome mutants. SHD, SCAR homology domain; WA, Wiskott-Aldrich homology 2, central, and acidic domain.

the *SCAR* genes, have undergone duplication and sequence diversification across multiple species. The diversification raises intriguing questions about potential functional differences of SCAR/WAVE subcomplexes. Recent results of investigations of the SCAR/WAVE downstream target, the ARP2/3 complex, have suggested the existence of functionally diverse ARP2/3 subcomplexes with varying subunit compositions (*30*). It is thus possible that different ARP2/3 subcomplexes, with varying subunit compositions, could selectively interact with distinct SCAR/WAVE subcomplexes. Such interactions may allow for greater diversity in actin regulation across various cellular contexts.

Although previous studies have identified SCAR mutants with visible phenotypes in *Oryza sativa* (*31*), *L. japonicus* (*32*), and *M. truncatula* (*11*), systematic functional studies on SCAR diversification have only been performed in *A. thaliana*. Our study expands this knowledge by showing that two *M. truncatula* SCAR proteins are not functionally interchangeable in *M. truncatula* or *A. thaliana* (Fig. 1). This contrasts with *A. thaliana* SCARs, which function interchangeably in trichome development when expressed under the same regulatory elements (*17*). To rule out a contribution of differential promoter activities among the different variants, all constructs in our study were driven under the same promoter. Furthermore, the chimeric proteins with domain swaps did retain their original activation domains (WA).

This study explores the functional similarities and differences of *MtAPI* and *MtHAPI1* in *M. truncatula* roots and *A. thaliana* leaves. We have not directly compared *MtHAPI1* with other previously assigned functions of *MtAPI* in *M. truncatula*, such as its role in susceptibility to oomycete root infection (*19*) or its requirement for nitrogen-fixing symbiosis (*27*). Future studies could benefit from the use of new genome editing tools to further explore *MtHAPI1* and *MtHAPI2* roles more comprehensively because there are no *M. truncatula* mutants available yet. However, our findings suggest a potential role for *MtHAPI1* in trichome development, a function distinct from that of *MtAPI*. Although *MtAPI* mutants do not exhibit trichome defects (*19*), the *rit1* mutant, which harbors a defective allele of *M. truncatula NAP1*—a single-copy SCAR/WAVE complex member—displays both root hair and trichome defects (*15*). Because *MtAPI* is not involved in trichome development, it is likely that this function may be mediated by *MtHAPI1*, *MtHAPI2*, or both, although further work is needed to confirm this hypothesis. These findings align with the idea that different SCAR/WAVE subcomplexes could serve tissue-specific roles, with *MtHAPI1* potentially involved in processes related to trichome formation.

One of our key findings shows that functional differences between *Mt*API and *Mt*HAPI1 are determined by two IDRs within the large central variable domain, rather than the SHD or WA domains (Fig. 2 and fig. S2). This highly variable central region, distinct in plant SCARs (*11*), represents an area for further investigation as it may contribute to the unique functionalities observed in legume species. IDRs can affect protein stability through both ubiquitin-dependent and ubiquitin-independent degradation by the proteasome (*33*, *34*). The overall structure, rather than a specific primary sequence, often defines this degradation function. It is therefore not unexpected that the amino acid sequences contributing to SCAR specificity can be variable. Rather than their sequence, it is the notable SCAR clade-specific absence or presence of the destabilizing segment in the IDR of several legume species (fig. S5) that suggests a functional diversification of SCAR homologs across species of the legume clade.

Although our findings provide valuable insights into the functional differences between *Mt*API and *Mt*HAPI1, one limitation of this study is the inability to definitively determine whether the observed functional differences in *M. truncatula* are due to variations in protein abundance or other factors. We confirmed that transgenic *M. truncatula* roots produced transgene transcripts. In the Arabidopsis work, we could detect fluorescent protein fusions but we were unable to detect mCitrine-tagged SCAR proteins in total protein extracts, likely due to their low abundance. This limitation highlights the need for further optimization of protein detection methods, particularly for SCAR proteins, which may require the presence of other SCAR/WAVE complex components for stability and proper detection.

We have identified a 42–amino acid segment within the central region of plant SCAR proteins as a major driver of the differential specificity of *Mt*API/HAPI1 (Figs. 3 and 4). Even a shorter 22–amino acid subsegment functions as a destabilizing element, affecting SCAR protein abundance (Fig. 4I). Our findings open avenues for future research to investigate how plants regulate SCAR protein abundance, which does not appear to be controlled by transcript levels or ubiquitination in this case (Fig. 4 and figs. S8 and S9). One potential mechanism that remains to be explored in the future is whether the 42–amino acid-dependent destabilization is underpinned by differential protein interactions. Furthermore, our results align with previous findings in *A. thaliana*, where SCAR/WAVE complex components transiently accumulate at the root hair initiation site, with abundance inversely correlated to root hair elongation speed (*28*). Although the specific segment we identified in *MtAPI* is not conserved in *AtSCAR2*, similar destabilizing elements may exist, providing a potential mechanism for rapid protein dissipation during root hair elongation.

In conclusion, this work has uncovered IDRs as the molecular basis for functional differences between two *M. truncatula* SCAR proteins, advancing our understanding of SCAR/WAVE complex specificity in plant development and plant-microbe interactions. These findings generate exciting directions for future research, particularly in identifying the biochemical mechanisms of SCAR protein abundance and functional regulation.

MATERIALS AND METHODS

Plant materials and growth conditions

Arabidopsis thaliana

Seeds of *A. thaliana Col-0* and *dis3-4* seeds were kindly provided by D. Szymanski. *A. thaliana* plants used for transformation, complementation assays, and propagation were grown in Levington F2 soil. The plants were maintained under constant light conditions (170 µmol m^{-2} s^{-1} PAR) at 21°C (day/night) temperature and 65% relative humidity. For confocal microscopy experiments, seedlings were sterilized with chlorine gas overnight and grown on ½ MS (pH 5.7) medium [0.22% (w/v) MURASHIGE & SKOOG MEDIUM (Duchefa Biochemie), 0.05% (w/v) MES monohydrate (MELFORD), and 1.2% (w/v) Plant Agar (Duchefa Biochemie)].

Medicago truncatula

Seeds of *M. truncatula* Jemalong A17 and *api* were propagated from previously described materials (*15*). For general propagation, *M. truncatula* plants were grown under long-day conditions (350 µmol m^{-2} s^{-1} PAR, 21°C for 16 hours; 0 µmol m^{-2} s^{-1} PAR, 17°C for 8 hours) at 65% humidity. The growth substrate used consisted of 45% Levington F2 soil, 45% Terra-Green stones/sand mixture (50:50), and 10% Perlite.

For hairy root transformations, *M. truncatula* plants were grown under long-day conditions with 16 hours of light at 20°C followed by 8 hours of darkness at ambient humidity.

Nicotiana benthamiana

For transient leaf infiltration assays and propagation, seeds of *N. benthamiana* were grown on Levington F2 soil under greenhouse conditions. The seeds are progenies of a laboratory cultivar from The Sainsbury Lab, Norwich, UK and originated from Australia (*35*).

Design of constructs and cloning

Primer design, sequence assembly, and analysis were performed using CLC Main workbench 20. Coding sequences (CDSs) for untagged *MtAPI* (*Medtr4g013235/MtrunA17_Chr4g0004861*) and *MtHAPI1* (*Medtr7g071440/MtrunA17_Chr7g0244031*) were synthesized in *pUC57* by GENEWIZ Inc. Chimeric *MtAPI* and *MtHAPI* CDSs were generated via Gibson assembly (see Fig. 2A). *MtAPI* and *MtHAPI1* regions were amplified using designated primers with overhangs for assembly: *MtAPI* region 1 (*MtAPI* bases 1 to 1548), primer pl_apiSHD_F_AG and API1_R_AG; *MtAPI* region 2 (*MtAPI* bases 1549 to 3153), primer API2_F_AG and API2_R_AG; *MtAPI* region 3 (*MtAPI* bases 3154 to 3690), primer API3.4.5._F_AG and API1.2.3_R_AG; *MtAPI* region 4 (*MtAPI* bases 3691 to 4278), primer API4_HAPI1_5_F_AG and apiMID_hapi1WH2_R_AG; *MtAPI* region 5 (*MtAPI* bases 4279 to 4722), primer hapi1MID_apiWH2_F_AG and apiWH2_pl_R_AG; *MtHAPI1* region 1 (*MtHAPI1* bases 1 to 1557), primer pl_hapi1SHD_F_AG and HAPI1_1_R_AG; *MtHAPI1* region 2 (*MtHAPI1* bases 1558 to 3054), primer HAPI1_2_F_AG and HAPI1_2_R_AG; *MtHAPI1* region 3 (*MtHAPI1* bases 3055 to 3594), primer HAPI1_3.4.5._F_AG and HAPI1_1.2.3._R_AG; *MtHAPI1* region 4 (*MtHAPI1* bases 3595 to 4044), primer HAPI1_4_API5_F_AG and hapi1MID_apiWH2_R_AG; *MtHAPI1* region 5 (*MtHAPI1* bases 4045 to 4488), and primers apiMID_hapiWH2_F_AG and hapi1WH2_pl_R_AG.

MtAPI and *MtHAPI1* mCitrine-tagged variants were synthesized with flanking Gateway-compatible attL1/2 sites and cloned into pUC57 by GenScript. The *mCitrine* CDS was inserted with a short N-terminal linker sequence (*linker-mCitrine*: GGAGGTGGAGGTGGAGCT) between *MtAPI* CDS bases 1812 and 1813. Four silent mutations introduced single-cut HpaI and BglII restriction sites flanking the insertion site (see data S1). Fourteen additional silent base pair mutations were introduced into the *MtAPI* CDS of API^{K517R}-*mCitrine*, API^{K518R}-*mCitrine*, API^{K520R}-*mCitrine*, API^{K547R}-*mCitrine*, API^{3xKtoR}-*mCitrine* and API^{4xKtoR}-*mCitrine*, $API^{\Delta A}$-*mCitrine*, $API^{\Delta B}$-*mCitrine*, $API^{\Delta C}$-*mCitrine*, $API^{\Delta AB}$-*mCitrine*, $API^{\Delta AC}$-*mCitrine*, $API^{\Delta BC}$-*mCitrine*, $API^{\Delta ABC}$-*mCitrine*, and API^{GS}-*mCitrine* to create single-cut restriction sites flanking: *MtAPI segment A* (BstBI/BsrGI); *segment B* (BspEI/Nhe); *segment C* (SpeI/SacII).

To generate KtoR mutant *Mt*API variants, we introduced the following additional mutations: K517R involved switching alanine 1550 and guanine 1551 (AG to GA); K518R involved changing alanine 1553 to guanine (A to G); K520R involved substituting alanine 1559 with guanine (A to G); K547R involved altering alanine 1640 to guanine (A to G).

To generate $API^{\Delta A}$-*mCitrine*, $API^{\Delta B}$-*mCitrine*, $API^{\Delta C}$-*mCitrine*, $API^{\Delta AB}$-*mCitrine*, $API^{\Delta AC}$-*mCitrine*, $API^{\Delta BC}$-*mCitrine*, $API^{\Delta ABC}$-*mCitrine*, and API^{GS}-*mCitrine*, 126 base pairs (bp) (*MtAPI segment A*: bases 1527 to 1654), 60 bp (*MtAPI segment B*: bases 3789 to 3850), and/or 87 bp (*MtAPI segment C*: bases 4035 to 4123) of the *MtAPI* CDS were deleted or swapped with corresponding GS linker sequences (*GS-linker A*: GGAGGTTCTGGTGGAGGTGGATCAGGTGGAGGATCTGCTGGCTCCGCTGCTGGTTCTGGCGAATTCGGAGGATCTGGAGGTGGAGGATCTGGAGGTGGATCTGCTGGATCTGCGCTGGTTCTGGA; *GS-linker B*: GGATCCGGTGGTGGAGGTTCTGGAGGTTCAGCTGGATCAGCTGCTGGAGGAGGTGGATCC; *GS-linker C*:GGATCAGGAGGTGGAGGTTCTGGAGGTGGATCAGCTGGATCAGCTGCTGGATCAGGTGAATTCGGAGGTTCTGGTGGAGGTGGATCA).

To create mCitrine-tagged *MtHAPI1* variants, the *linker-mCitrine* CDS was inserted between *MtHAPI1* bases 1704 and 1705. Eight silent base pair mutations were introduced into the *MtHAPI1* CDS to generate single-cut restriction sites flanking the *MtAPI segment A* (ClaI/BssHII), *linker-mCitrine* (BspEI/PmlI), *MtAPI segment B* (SpeI/XhoI), and *MtAPI segment C* (BstBI/MfeI) insertion sites. For generating $HAPI1^{+ABC}$-*mCitrine* and $HAPI1^{GS}$-*mCitrine*, *MtAPI segments* or *GS-linker* sequences were inserted as follows: *MtAPI segment A* or *GS-linker A* (126 bp between *MtHAPI1* bases 1536 and 1537), *MtAPI segment B* or *GS-linker B* (60 bp, between *MtHAPI1* bases 3690 and 3691), and *MtAPI segment C* or *GS-linker C* (87 bp between *MtHAPI1* bases 3879 and 3880.

All *42aa-mCitrine* derived constructs feature a variable N-terminal sequence, followed by a *shortAPI-linker-mCitrine* sequence (*MtAPI* bases 1655 to 1812 plus "GGAGGTGGAGGTGGAGCT" linker; in total 177 bp) and *mCitrine* with a stop codon. *42aa-mCitrine* was amplified from *pUC57-API-mCitrine* using primers SB295 and SB296. *GS-mCitrine* was amplified from *pUC57-*API^{GS}*-mCitrine* using primers SB323 and SB296. *41aa-mCitrine* was amplified from *pKGW-pAtUBQ-42aa-mCitrine* using primers SB329 and SB296. *22-43aa-mCitrine* was amplified from *pKGW-pAtUBQ-42aa-mCitrine* using primers SB324 and SB296. *31-43aa-mCitrine* was amplified from *pKGW-pAtUBQ-42aa-mCitrine* using primers SB325 and SB296. *22-30aa-mCitrine* was amplified from *pDONR221-31-43aa-mCitrine* with primers SB343 and SB296. *4xKtoR-mCitrine* was amplified from *pUC57_KAN_API_K4xR_mCitrine* with primers SB342 and SB296. Polymerase chain reactions (PCRs) were performed using Phusion DNA polymerase (New England Biolabs Inc., UK).

The CDSs of *1-21aa-mCitrine*, *4xSTtoA-mCitrine*, and *4xSTtoD-mCitrine* were synthesized with Gateway-compatible attL1/2 sites and cloned into pUC57 by GenScript. *1-21aa-mCitrine* includes a start codon with *MtAPI* bases 1528 to 1587 fused to the *shortAPI-linker-mCitrine* sequence. *4xSTtoA-mCitrine* and *4xSTtoD-mCitrine* include a start codon with *MtAPI segment A* (bases 1527 to 1654) fused to the *shortAPI-linker-mCitrine* sequence. *4xSTtoA-mCitrine* features the following mutations: AGCA to GCAG (MtAPI bases 1588 to 1591), alanine 1606 and thymine 1612 to guanines, and thymine 1638 to cytosine. *4xSTtoD-mCitrine* features the following mutations: AGCAC to GATGA (MtAPI bases 1588 to 1592), ACA to GAT (MtAPI bases 1606 to 1608), and TCA to GAT (MtAPI bases 1612 to 1614).

All entry and destination vectors were validated using diagnostic restriction digest and Sanger sequencing (Source BioScience). Destination clones were assembled by recombining pUC57 gateway compatible *MtAPI* and *MtHAPI1* variants with *pENTR4_1_prAtUBQ3* or *pENTR4_1_prMtAPI* and *pENTR_p2rp3_T35STerm* into *pKGW-RR-MGW* destination vector with LR Clonase Plus (Thermo Fisher Scientific) (*15*). All primer sequences and constructs used in this study are detailed in tables S1 and S2, respectively. A fasta file containing the vector and CDSs is available as data S1.

Generation of transgenic plants

A. thaliana stable transformations

Destination vectors were introduced into *Agrobacterium tumefaciens* strain *GV3101* (resistant to tetracycline, rifampicin, and gentamicin)

and transformed into *A. thaliana* accession *Col-0* and *dis3-4*. Primary transformants were screened for DsRed fluorescence at the seed and seedlings stage (5 days of growth on soil). Screening was performed using a portable NIGHTSEA model SFA with the GR-Green wavelength set (excitation: 510 to 540 nm; emission: 600-nm longpass). At least three independent transgenic lines were propagated for each construct and background.

M. truncatula *root transformations*

Destination vectors were introduced into *Agrobacterium rhizogenes* strain *Arqua1193* (resistant to rifampicin and carbenicillin) and transformed into *A17* and *api* seedling roots according to Limpens *et al.* (*36*). Transformed roots were subsequently grown on Fahraeus medium for 3 weeks.

N. benthamiana *leaf infiltrations*

To transiently express proteins, destination vectors were introduced into *A. tumefaciens* strain *GV3101* (resistant to tetracycline, rifampicin, and gentamicin). Overnight bacterial cultures were resuspended in agroinfiltration medium [10 mM $MgCl_2$, 10 mM MES (pH 5.7), and 200 μM acetosyringone] to an OD (optical density) of 0.6. Bacterial suspensions were injected into the abaxial side of 4-week-old *N. benthamiana* leaves. Expression of constructs was analyzed 3 days postinfiltration.

Bioinformatic analysis of protein sequence conservation and intrinsic disorder

MtAPI/HAPI1 amino acid conservation barcode

To assess amino acid conservation, the protein sequences of *Mt*API and *Mt*HAPI1 were aligned using the EMBOSS Needle pairwise alignment tool (https://ebi.ac.uk/jdispatcher/psa/emboss_needle). Alignment results, reflecting the degree of similarity or mismatch between residues in the form of pipe/colon/period and space symbols, were translated into color-coded stripes using RStudio. The color code was as follows: black (pipe = identical residue), dark gray (colon = highly similar amino acid), light gray (period = moderately similar amino acid), and white (space = alignment gap). The percentage of identical residues in each region was found the using NCBI BLASTp search (https://blast.ncbi.nlm.nih.gov/Blast.cgi).

Intrinsic disorder

Intrinsically disordered protein regions (IUPRED3) and disordered protein binding regions (ANCHOR2) were predicted using the web server IUPRED3 (https://iupred3.elte.hu/). Sequences were input into IUPRED3 to obtain disorder scores, which were then plotted as line graphs using RStudio.

Legume MtAPI/HAPI like protein alignments

Legume *Mt*API and *Mt*HAPI1-like sequences were aligned using the "Create Alignment" function in CLC Main Workbench 20 with settings of gap open cost 10, gap extension cost 1, and the "very accurate" alignment algorithm. The resulting alignment graphics were imported into Inkscape, where text styles were adjusted to match the overall figure design.

Phylogenetic analysis

Legume SCAR protein sequences were retrieved from publicly available legume reference genomes using a BLASTp search with the *At*SCAR2 sequence (*At2G38440*; Tair) as query. Sequences for *Lupinus angustifolius*, *Glycine max*, *Phaseolus vulgaris*, *Vigna angularis*, and *Trifolium pratense* were obtained from the EnsemblPlants platform (http://plants.ensembl.org/index.html); for *Nissolia schottii*, *Arachis hypogaea*, *Cajanus cajan*, and *Lablab purpureus* from the SymDB database (https://polebio.lrsv.ups-tlse.fr/symdb/web/); for *L. japonicus MG20* from Lotus Base (https://lotus.au.dk); and for *M. truncatula* from the Medicago A17 genome browser (https://medicago.toulouse.inra.fr/MtrunA17r5.0-ANR/). Full-length sequences were aligned and subsequently automatically trimmed using the bioconda packages "mafft" (version 7.471) (https://anaconda.org/bioconda/mafft) (*37*) and "trimAl" (version 1.4.1) (https://trimal.readthedocs.io/en/latest/) (*38*). Phylogenetic trees were constructed using the bioconda package "IQ-TREE" (version 2.0.3) (*39*) with maximum likelihood and bootstrapping (1000Ufboot+SH-aLRT) and identified the best fitting substitution models: "JTT+G4" for Fig. 1A and "HIVb+F+I+G4" for fig. S4A. Trees were visualized with the online tool "interactive Tree Of Life" (iTOL version 6.9.1; https://itol.embl.de/) (*40*) and stylistically modified for figure presentation using Inkscape.

Microscopic analysis of root hair and trichome morphology

M. truncatula *root hair length analysis*

Three weeks posttransformation, epifluorescence microscopy images of DsRed-expressing *M. truncatula* roots were captured using a Leica M165 FC Fluorescent Stereomicroscope with a DFC310FX camera and DSR filter (10447412). All images were taken at the same magnification (including a reference scale) with the Leica Application Suite Software (version 4.8.0). Root hair length was quantified using the ROI manager and Freehand line tools in ImageJ2. The image scales were globally calibrated using the SetScale function. For each genotype, the length of 20 root hairs from five independently transformed roots ($n = 100$) was measured in millimeters. Data normality was assessed using the Shapiro-Wilk test, and for P values below 0.5, the Kruskal-Wallis test with Bonferroni P value adjustment (alpha = 0.05) was applied for post hoc analysis. Box plots were generated in R. Images were adjusted for grayscale, brightness, and contrast using GIMP, and figure panels were assembled in Inkscape with manually added scale bars based on the reference scale. Independent transformations/experiments were carried out at least twice for each analyzed construct. One representative experiment was chosen for the final figures.

A. thaliana *trichome branch length analysis*

Scanning electron micrographs of *A. thaliana* leaves and trichomes were captured using the Hitachi tabletop microscope TM4000 Plus with the provided software. Leaves of 9-day-old *A. thaliana* plants, grown on soil, were detached and mounted on sample stubs with water droplets. The cooling stage was set to −25°C with low vacuum applied upon sample insertion. BSE (backscatter) detector mode was used with an accelerating voltage of 15 kV. Whole leaf images were captured at 30x magnification and trichome close-ups at 150x magnification, with corresponding scale bars calculated by the software. Brightness, contrast, and cropping adjustments were made using GIMP. Three images from independent transgenic lines per genotype were analyzed. For each image, five representative trichomes were selected, and the length of each trichome branch was measured from branch points to tip using the Freehand Line tool in ImageJ2. The shortest branch ratio was determined by dividing the length of the shortest branch by the longest branch for each trichome (1 = equal length; $n = 15$). These data were filtered, analyzed, and visualized as box plots In R. Final figure panels, including representative trichome images, scale bars, and barplots were assembled using Inkscape. One representative experiment was chosen for the figures, but each construct was analyzed in the different background in at least three

independently transformed Arabidopsis lines and trichome morphology was analyzed at least three times in the T1 and T2 generation.

Localization and expression analysis via confocal microscopy

For confocal imaging of *A. thaliana* root cells and *N. benthamiana* pavement cells, samples were mounted in water on glass slides (Fisher, 1 to 1.2 mm) and covered with coverslips (Epredia, #1.5). Imaging was performed using a LeicaTCS SP8 upright confocal microscope, equipped with a white light laser system.

Imaging of A. thaliana *seedling roots*

Five-day-old stably transformed *A. thaliana* seedlings, grown on ½ MS (pH 5.7), were mounted and screened for root fluorescence. Single-plain root cell images were acquired with HC PL APO CS2 63w/1.20 water immersion objective and the following laser/detector settings: sequential scan; sequence1 (mCitrine): excitation with WLL line 518 nm: 70% intensity, detection with HyD1: 523 to 535 nm gain (%) 500, time gating on, 0.3 to 6 ns; sequence 2 (DsRed): excitation WLL line 570 nm: 5% intensity, detection with PMT3 577-602 nm gain (V) 890.8 offset: −0.02. Unidirectional scan, speed: 200 Hz, line averaging: 8, pinhole: 1 airy unit, zoom: 3. The representative images shown in Fig. 3 (H and J) were chosen from an experiment where the root tips, and leaves of two T2 seedlings per genotype were imaged. The fluorescence signal analysis was repeated at least once for each genotype in different experiments.

Imaging of N. benthamiana *pavement cells*

Three days after transformation, leaf discs (cork borer size three) of six independently transformed plants (biological replicates) were analyzed for fluorescence. Single-plane, 16-bit images of the pavement cell were acquired with the following settings: sequential scan; sequence 1 (mCitrine): excitation 515 nm: 0.5 to 10% intensity, detection with HyD1: 518 to 537 nm gain (%) 500, time gating 0.6 to 6 ns; sequence 2 (DsRed): excitation 560 nm: 0.5 to 10% intensity, detection with HyD5 574 to 598 nm gain (%) 500, time gating 0.4 to 6 ns. Unidirectional scan, speed: 600 Hz, line averaging: 8, pinhole: 1 airy unit, zoom: 1. Laser intensities were optimized between experiments while maintaining consistent settings within each experiment. To calculate mCitrine/DsRed ratios, the segment and ratio tool of the FRETENATOR2 beta version [https://github.com/JimageJ/FRETENATOR2; based on Rowe *et al.*, 2023 (*41*)] FIJI plug-in was used. The plug-in automatically segments images and calculates ratios for the segmented pixels areas. Settings were chosen as follows: Denominator ("Donor") and Segmentation channel: DsRed; Numerator ("Acceptor") channel: mCitrine; Gaussian segmentation, maximum intensity: 65,534 without background subtraction; pixel by pixel analysis: on. For each genotype, mean ratio measurements were taken from one image per six independently transformed plants, using the "Maximum z of emission ratio z projection X1000" images ($n = 6$). The mean ratios were divided by 1000 and plotted using R. Each construct was tested at least twice in independent experiments. One representative experiment was chosen for the final figures.

Quantitative reverse transcription PCR analysis

For each construct, three leaf discs (cork borer size five) were collected from a single transformed *N. benthamiana* leaf and immediately frozen in liquid nitrogen. As negative control, three leaf discs per biological replicate were also harvested from untransformed leafs. A total of six biological replicates per genotype were analyzed. RNA extraction was carried out following the manufacturer's protocol for the RNEasy Plant Mini Kit (QIAGEN), using buffer RLC. For each sample, 4 µg of total RNA was used as a template for cDNA synthesis, which was performed using the Transcriptor First Strand cDNA Synthesis Kit (Roche). Quantitative reverse transcription PCR was conducted using 2.5 µl of a 1:8 dilution of the first-strand cDNA and LightCycler 480 SYBR Green I Master mix, following the manufacturer's instructions (Roche). *mCitrine* transcript levels were analyzed using primers SB268 and SB269 (table S1). The *N. benthamiana* genes *NtL23* (*Niben101Scf01444g02009*) and *NtFBOX* (*Niben101Scf04495g02005*) were chosen as constitutively expressed reference genes (*42*). *NtL23* was amplified using primers SB304 and SB305 (table S1). *NtFBOX* was amplified using primers SB306 and SB307 (table S1). The expression of *mCitrine* was normalized to *NtL23* and *NtFBOX* expression using the efficiency-corrected ΔΔCq method. The data were visualized using R software. The quantitative PCR (qPCR) analysis of the *N. benthamiana* samples was repeated twice independently.

SDS-PAGE and immunoblot

For each construct, two leaf discs (cork borer size five) were collected from six independently transformed *N. benthamiana* plants, pooled, and immediately frozen in liquid nitrogen. The experiment was performed twice. The frozen tissue was ground into a fine powder with a porcelain pestle and mortar. To this powder, 500 µl of lysis buffer [GTEN: 50 mM tris-HCl (pH7.5), 10% (v/v) glycerol, 1 mM EDTA, 150 mM NaCl, supplemented with 2% (w/v) polyvinylpolypyrrolidone, 0.1% (v/v) Tween 20, phosphatase inhibitors (Sigma-Aldrich, P5726 and P0044), and plant protease inhibitors (Sigma-Aldrich, P9599)] was added. The mixture was incubated on ice for 10 minutes. Following a 5-minute centrifugation at maximum speed (4°C), 400 µl of the supernatant was mixed with 4x Laemmli buffer containing β-mercaptoethanol and boiled at 95°C for 5 min.

SDS–polyacrylamide gel electrophoresis (PAGE) was carried out using 4 to 20% Mini-PROTEAN TGX Precast protein gels (Bio-Rad). After electrophoresis, proteins were transferred onto a 0.45-µm PVDF (polyvinylidene difluoride) membrane (Immobilon, Merck). The membranes were stained with a 1:1 mix of glacial acetic acid and Ponceau Red (Bio-Rad) for protein visualization, followed by three brief washes in deionized water. Membranes were blocked for 1 hour in a TBS-T buffer [20 mM Tris base, 150 mM NaCl, and 0.1% (v/v) Tween 20] containing 5% (w/v) milk powder. Subsequent incubations (for 1 hour) were carried out in primary and secondary antibodies diluted in the same blocking solution. After each incubation step, membranes were washed three times for 10 min with TBS-T buffer. The following antibodies and dilutions were used: mouse anti-GFP (B2 sc-9996, Santa Cruz biotechnology) 1:2500, rabbit anti–red fluorescent protein (RFP) (AB62341, Abcam), m-IgG Fc binding protein horseradish peroxidase (HRP) (sc-542732, Santa Cruz Biotechnology) 1:5000, and goat anti-rabbit IgG HRP (AB205718, Abcam) 1:5000. Protein bands were detected using chemiluminescence with ECL Plus (Thermo Fisher Scientific) and visualized on an Amersham Imager 600.

Protein extraction, immunoprecipitation, and mass spectrometry analysis

Three leaves from *N. benthamiana* plants, transformed with either *mCitrine* or *42aa-mCitrine*, were harvested 72 hours postagroinfiltration. The leaves were flash frozen in liquid nitrogen and ground into a fine powder using porcelain pestles and mortars. Proteins were extracted by adding 5 ml of lysis buffer [GTEN: 50 mM tris-HCl, (pH 7.5), 10% (v/v) glycerol, 1 mM EDTA, 150 mM NaCl, supplemented with 2% (w/v) polyvinylpolypyrrolidone, 0.1% (v/v) Tween 20, phosphatase inhibitors (Sigma-Aldrich, P5726 and P0044), and plant protease

inhibitors (Sigma-Aldrich P9599)] to the leaf powder. For immunoprecipitation (IP), 60 µl of GFP-Trap agarose bead slurry (Chromotek) was added to each sample after centrifugation at maximum speed for 5 min at 4°C. The samples were incubated for 2 hours at 4°C with slow rotation. Following incubation, the samples were centrifuged at 2000 rpm for 2 min at 4°C, and the resulting pellet was washed five times with 1 ml of IP buffer [GTEN, supplemented with 0.1% (v/v) Tween 20]. After the final wash, the supernatant was removed, and 20 µl of IP buffer along with 10 µl of 4x Laemmli buffer (supplemented with β-mercaptoethanol) was added. The sample proteins were denatured by heat treatment at 95°C for 5 min. SDS-PAGE was performed using 4–20% Mini-PROTEAN TGX Precast protein gels (Bio-Rad). After electrophoresis, the gel was stained overnight in 20 ml of SimplyBlue (Invitrogen) staining solution, supplemented with 2 ml of 20% NaCl in water (w/v).

Protein bands, corresponding to mCitrine and 42aa-mCitrine, were excised and subjected to in-gel reduction and alkylation, followed by trypsin digestion and peptide extraction by the Cambridge Proteomics Centre. The resulting peptides were analyzed by liquid chromatography–tandem mass spectrometry, and posttranslational modification identification was performed using the MASCOT search algorithm with *N. benthamiana* v1.01 gene models (https://solgenomics.net). In addition, *Mt*API segment A (*Mt*API amino acids 510 to 551) was also analyzed for potential posttranslational modification sites with the web server application MusiteDeep (https://musite.net/), which uses a deep learning framework for protein posttranslational modification site prediction. The mass spectrometry experiment was performed once.

Usage of generative AI and AI-assisted technologies

ChatGPT-4 turbo was used to check the manuscript for grammar mistakes, improve the phrasing of the sentences and shorten figure legends. The following prompts were used: "Please, help me to improve the following sentence/paragraph/figure legend" and "How can I shorten this figure legend." After using ChatGPT, the authors reviewed and edited the content as needed and take full responsibility for the content of the publication.

Software versions

The following software versions were used: RStudio 2022.02.1 with R 4.1.3.; Inkscape 1.2.2; ImageJ2 software version 2.14.0 including FIJI plugins; GNU image manipulation program (GIMP version 2.10.30).

Accession numbers/identifiers

The following accession numbers/identifiers were used: *Mt*API (Medtr4g013235/MtrunA17_Chr4g0004861); *Mt*HAPI1 (Medtr7g071440/MtrunA17_Chr7g0244031); *At*SCAR2/DIS3 (AT2G38440); *At*SCAR1 (AT2G34150), AtSCAR3 (AT1G29170), and AtSCAR4 (AT5G01730); *At*NAP1 (AT2G35110); *Nt*L23 (Niben101Scf01444g02009); *Nt*FBOX (Niben101Scf04495g02005).

Supplementary Materials

The PDF file includes:

Figs. S1 to S10
Tables S1 to S4
Legend for data S1

Other Supplementary Material for this manuscript includes the following:

Data S1

REFERENCES AND NOTES

1. Z. Winter, K. Bellande, J. E. M. Vermeer, Divided by fate: The interplay between division orientation and cell shape underlying lateral root initiation in Arabidopsis. *Curr. Opin. Plant Biol.* **74**, 102370 (2023).
2. C. Goldy, M. C. Caillaud, Connecting the plant cytoskeleton to the cell surface via the phosphoinositides. *Curr. Opin. Plant Biol.* **73**, 102365 (2023).
3. S. Kumar, T. Jeevaraj, M. H. Yunus, S. Chakraborty, N. Chakraborty, The plant cytoskeleton takes center stage in abiotic stress responses and resilience. *Plant Cell Environ.* **46**, 1 (2023).
4. D. D. Bhandari, F. Brandizzi, Logistics of defense: The contribution of endomembranes to plant innate immunity. *J. Cell Biol.* **223**, 6 (2024).
5. R. D. Mullins, J. A. Heuser, T. D. Pollard, The interaction of Arp2/3 complex with actin: Nucleation, high affinity pointed end capping, and formation of branching networks of filaments. *Proc. Natl. Acad. Sci. U.S.A.* **95**, 6181–6186 (1998).
6. F. Fäßler, G. Dimchev, V. V. Hodirnau, W. Wan, F. K. M. Schur, Cryo-electron tomography structure of Arp2/3 complex in cells reveals new insights into the branch junction. *Nat. Commun.* **11**, 6437 (2020).
7. J. Mathur, N. Mathur, B. Kernebeck, M. Hülskamp, Mutations in actin-related proteins 2 and 3 affect cell shape development in Arabidopsis. *Plant Cell* **15**, 1632–1645 (2003).
8. S. El-Din El-Assal, J. Le, D. Basu, E. L. Mallery, D. B. Szymanski, DISTORTED2 encodes an ARPC2 subunit of the putative *Arabidopsis* ARP2/3 complex. *Plant J.* **38**, 526–538 (2004).
9. S. Li, L. Blanchoin, Z. Yang, E. M. Lord, The putative Arabidopsis arp2/3 complex controls leaf cell morphogenesis. *Plant Physiol.* **132**, 2034–2044 (2003).
10. P. A. Harries, A. Pan, R. S. Quatrano, Actin-related protein2/3 complex component ARPC1 is required for proper cell morphogenesis and polarized cell growth in *Physcomitrella patens*. *Plant Cell* **17**, 2327–2339 (2005).
11. M. Yanagisawa, C. Zhang, D. B. Szymanski, ARP2/3-dependent growth in the plant kingdom: SCARs for life. *Front. Plant Sci.* **4**, 166 (2013).
12. D. Basu, J. Le, D. El-Essal Sel, S. Huang, C. Zhang, E. L. Mallery, G. Koliantz, C. J. Staiger, D. B. Szymanski, DISTORTED3/SCAR2 is a putative Arabidopsis WAVE complex subunit that activates the Arp2/3 complex and is required for epidermal morphogenesis. *Plant Cell* **17**, 502–524 (2005).
13. J. F. Uhrig, M. Mutondo, I. Zimmermann, M. J. Deeks, L. M. Machesky, P. Thomas, S. Uhrig, C. Rambke, P. J. Hussey, M. Hülskamp, The role of *Arabidopsis SCAR* genes in ARP2-ARP3-dependent cell morphogenesis. *Development* **134**, 967–977 (2007).
14. S. Djakovic, J. Dyachok, M. Burke, M. J. Frank, L. G. Smith, BRICK1/HSPC300 functions with SCAR and the ARP2/3 complex to regulate epidermal cell shape in *Arabidopsis*. *Development* **133**, 1091–1100 (2006).
15. A. Miyahara, J. Richens, C. Starker, G. Morieri, L. Smith, S. Long, J. A. Downie, G. E. Oldroyd, Conservation in function of a SCAR/WAVE component during infection thread and root hair growth in *Medicago truncatula*. *Mol. Plant Microbe Interact.* **23**, 1553–1562 (2010).
16. Y. Li, K. Sorefan, G. Hemmann, M. W. Bevan, Arabidopsis *NAP* and *PIR* regulate actin-based cell morphogenesis and multiple developmental processes. *Plant Physiol.* **136**, 3616–3627 (2004).
17. C. Zhang, E. L. Mallery, J. Schlueter, S. Huang, Y. Fan, S. Brankle, C. J. Staiger, D. B. Szymanski, *Arabidopsis* SCARs function interchangeably to meet actin-related protein 2/3 activation thresholds during morphogenesis. *Plant Cell* **20**, 995–1011 (2008).
18. C. I. Jörgens, N. Grünewald, M. Hülskamp, J. F. Uhrig, A role for ABIL3 in plant cell morphogenesis. *Plant J.* **62**, 925–935 (2010).
19. A. Gavrin, T. Rey, T. A. Torode, J. Toulotte, A. Chatterjee, J. L. Kaplan, E. Evangelisti, H. Takagi, V. Charoensawan, D. Rengel, E. P. Journet, F. Debelle, F. de Carvalho-Niebel, R. Terauchi, S. Braybrook, S. Schornack, Developmental modulation of root cell wall architecture confers resistance to an oomycete pathogen. *Curr. Biol.* **30**, 4165–4176.e5 (2020).
20. M. Frank, C. Egile, J. Dyachok, S. Djakovic, M. Nolasco, R. Li, L. G. Smith, Activation of Arp2/3 complex-dependent actin polymerization by plant proteins distantly related to Scar/WAVE. *Proc. Natl. Acad. Sci. U.S.A.* **101**, 16379–16384 (2004).
21. Y. Miao, T. Tipakornsaowapak, L. Zheng, Y. Mu, E. Lewellyn, Phospho-regulation of intrinsically disordered proteins for actin assembly and endocytosis. *FEBS J.* **285**, 2762–2784 (2018).
22. C. Haynes, C. J. Oldfield, F. Ji, N. Klitgord, M. E. Cusick, P. Radivojac, V. N. Uversky, M. Vidal, L. M. Iakoucheva, Intrinsic disorder is a common feature of hub proteins from four eukaryotic interactomes. *PLoS Comput. Biol.* **2**, e100 (2006).
23. E. S. Groban, A. Narayanan, M. P. Jacobson, Conformational changes in protein loops and helices induced by post-translational phosphorylation. *PLoS Comput. Biol.* **2**, e32 (2006).
24. A. Y. Pollitt, R. H. Insall, WASP and SCAR/WAVE proteins: The drivers of actin assembly. *J. Cell Sci.* **122**, 2575–2578 (2009).
25. M. Evangelista, B. M. Klebl, A. H. Tong, B. A. Webb, T. Leeuw, E. Leberer, M. Whiteway, D. Y. Thomas, C. Boone, A role for myosin-I in actin assembly through interactions with Vrp1p, Bee1p, and the Arp2/3 complex. *J. Cell Biol.* **148**, 353–362 (2000).

26. D. Feliciano, T. O. Tolsma, K. B. Farrell, A. Aradi, S. M. Di Pietro, A second Las17 monomeric actin-binding motif functions in Arp2/3-dependent actin polymerization during endocytosis. *Traffic* **16**, 379–397 (2015).
27. A. Teillet, J. Garcia, F. de Billy, M. Gherardi, T. Huguet, D. G. Barker, F. de Carvalho-Niebel, E. P. Journet, *api*, A novel *Medicago truncatula* symbiotic mutant impaired in nodule primordium invasion. *Mol. Plant Microbe Interact.* **21**, 535–546 (2008).
28. S. Chin, T. Kwon, B. R. Khan, J. A. Sparks, E. L. Mallery, D. B. Szymanski, E. B. Blancaflor, Spatial and temporal localization of SPIRRIG and WAVE/SCAR reveal roles for these proteins in actin-mediated root hair development. *Plant Cell* **33**, 2131–2148 (2021).
29. J. Dyachok, M. R. Shao, K. Vaughn, A. Bowling, M. Facette, S. Djakovic, L. Clark, L. Smith, Plasma membrane-associated SCAR complex subunits promote cortical F-actin accumulation and normal growth characteristics in *Arabidopsis* roots. *Mol. Plant* **1**, 990–1006 (2008).
30. E. Bellinvia, J. Garcia-Gonzalez, P. Cifrova, J. Martinek, L. Sikorova, L. Havelkova, K. Schwarzerova, CRISPR-Cas9 Arabidopsis mutants of genes for ARPC1 and ARPC3 subunits of ARP2/3 complex reveal differential roles of complex subunits. *Sci. Rep.* **12**, 18205 (2022).
31. J. Bai, X. Zhu, Q. Wang, J. Zhang, H. Chen, G. Dong, L. Zhu, H. Zheng, Q. Xie, J. Nian, F. Chen, Y. Fu, Q. Qian, J. Zuo, Rice TUTOU1 encodes a suppressor of cAMP receptor-like protein that is important for actin organization and panicle development. *Plant Physiol.* **169**, 1179–1191 (2015).
32. L. Qiu, J. S. Lin, J. Xu, S. Sato, M. Parniske, T. L. Wang, J. A. Downie, F. Xie, SCARN a novel class of SCAR protein that is required for root-hair infection during legume nodulation. *PLOS Genet.* **11**, e1005623 (2015).
33. J. Takeuchi, H. Chen, P. Coffino, Proteasome substrate degradation requires association plus extended peptide. *EMBO J.* **26**, 123–131 (2007).
34. S. Prakash, L. Tian, K. S. Ratliff, R. E. Lehotzky, A. Matouschek, An unstructured initiation site is required for efficient proteasome-mediated degradation. *Nat. Struct. Mol. Biol.* **11**, 830–837 (2004).
35. J. Bally, H. Jung, C. Mortimer, F. Naim, J. G. Philips, R. Hellens, A. Bombarely, M. M. Goodin, P. M. Waterhouse, The rise and rise of *Nicotiana benthamiana*: A plant for all reasons. *Annu. Rev. Phytopathol.* **56**, 405–426 (2018).
36. E. Limpens, R. Mirabella, E. Fedorova, C. Franken, H. Franssen, T. Bisseling, R. Geurts, Formation of organelle-like N2-fixing symbiosomes in legume root nodules is controlled by DMI2. *Proc. Natl. Acad. Sci. U.S.A.* **102**, 10375–10380 (2005).
37. J. Rozewicki, S. Li, K. M. Amada, D. M. Standley, K. Katoh, MAFFT-DASH: Integrated protein sequence and structural alignment. *Nucleic Acids Res.* **47**, W5–W10 (2019).
38. S. Capella-Gutierrez, J. M. Silla-Martinez, T. Gabaldon, trimAl: A tool for automated alignment trimming in large-scale phylogenetic analyses. *Bioinformatics* **25**, 1972–1973 (2009).
39. L. T. Nguyen, H. A. Schmidt, A. von Haeseler, B. Q. Minh, IQ-TREE: A fast and effective stochastic algorithm for estimating maximum-likelihood phylogenies. *Mol. Biol. Evol.* **32**, 268–274 (2015).
40. I. Letunic, P. Bork, Interactive Tree of Life (iTOL) v6: Recent updates to the phylogenetic tree display and annotation tool. *Nucleic Acids Res.* **52**, W78–W82 (2024).
41. J. Rowe, M. Grange-Guermente, M. Exposito-Rodriguez, R. Wimalasekera, M. O. Lenz, K. N. Shetty, S. R. Cutler, A. M. Jones, Next-generation ABACUS biosensors reveal cellular ABA dynamics driving root growth at low aerial humidity. *Nat. Plants* **9**, 1103–1115 (2023).
42. D. Liu, L. Shi, C. Han, J. Yu, D. Li, Y. Zhang, Validation of reference genes for gene expression studies in virus-infected *Nicotiana benthamiana* using quantitative real-time PCR. *PLOS ONE* **7**, e46451 (2012).

Acknowledgments: We thank D. Szymanski for providing us with *A. thaliana Col* and *dis3-4* seeds, J. Rowe for help with the installation and usage of the Fretenator plugin, and R. Kowalczyk for technical assistance. We are also grateful to P. Carella and A. Wanke for discussion and critical reading of the manuscript. **Funding:** This work was funded by the Gatsby Charitable Foundation (GAT3395/GLD; S.S.), the European Research Council (ERC-2014-STG, H2020, and 637537; S.S.), and the Royal Society (UF110073 and UF160413; S.S.). **Author contributions:** Conceptualization: S.B., A.G., and S.S. Methodology: S.B., A.G., and M.M. Investigation: S.B., A.G., M.M., G.C., and A.U. Validation: S.B., A.G., M.M., and A.U. Formal analysis: S.B., A.G., M.M., and A.U. Data curation: S.B. Visualization: S.B. Supervision: S.B., A.G., and S.S. Project administration: S.S. and S.B. Writing—original draft: S.B., A.G., and S.S. Writing—review and editing: S.B., G.C., and S.S. Funding acquisition: S.S. **Competing interests:** The authors declare that they have no competing interests. **Data and materials availability:** All data needed to evaluate the conclusions in the paper are present in the paper and/or the Supplementary Materials.

Submitted 4 October 2024
Accepted 18 April 2025
Published 21 May 2025
10.1126/sciadv.adt6107